



Effect of Substrate Surface Texture Shapes on the Adhesion of Plasma-Sprayed Ni-Based Coatings

Xianghua Zhan¹ · Yancong Liu^{1,2} · Peng Yi¹ · Wenlong Feng¹ · Zhihao Feng¹ · Yanchao Jin¹

Submitted: 9 August 2020 / in revised form: 5 November 2020 / Accepted: 9 November 2020 / Published online: 25 November 2020
© ASM International 2020

Abstract The bonding of thermal-sprayed coatings largely depends on the substrate surface morphology. This study examines the effect of the substrate surface texture shapes on the adhesion strength of coatings. For that, it used plasma-sprayed Ni-based MoS₂ coatings deposited on grit-blasted and laser-textured surfaces, and investigated the coating bonding strength (ASTM 633 pull-off test), and cross-sectional and fracture morphologies, as well as phase compositions and element distribution. The results showed that the surface texture shape has a significant effect on the improvement of coating adhesion. The coatings deposited on sinusoidal-textured surfaces had the highest adhesion strength (50.0 MPa), followed by coatings deposited on groove-textured surfaces, while dimple and dimple–groove textures resulted in the lowest coating adhesion strength. The coating fracture analysis revealed that cohesive failure occurred mainly at the texture positions, while adhesive failure occurred almost always in plain areas. Therefore, it could be concluded that, in the conditions of this study, the existence of plain areas and dimple textures did not improve coating adhesion. Factors such as coating bond mode, contact area ratio, and coating deposition quality should be comprehensively considered in texture design to improve coating adhesion.

Keywords atmospheric plasma spray · coating adhesion · laser texturing · pull-off test · texture shape

Introduction

The good adhesion of solid lubricants to substrate surfaces is necessary to ensure the presence of these lubricants on friction pair surfaces even at high shear stresses (Ref 1). Solid lubricant coatings have attracted increasing attention in recent years due to their excellent film-to-substrate bonding performance and extremely low friction and wear coefficients under certain or highly controlled test conditions (Ref 2). Numerous methods, including powder metallurgy, vapor deposition, thermal spray, and cold spray, have been developed for the fabrication of strongly bonded coatings on various substrates (Ref 3–6). Plasma spraying is one of the most commonly used techniques (Ref 7). The bond strength of coatings strongly depends on substrate topography, coating temperature gradient, residual stresses, and surface composition (Ref 8–10). Grit blasting (GB) is the most commonly used pretreatment method for plasma spraying to roughen substrate surfaces. However, GB has several limitations, such as surface damage with severe surface plastic deformation and microcracks, grit particle inclusion, and relatively weak adhesion between coatings and substrates (Ref 11, 12). Hence, new techniques that can overcome these shortcomings in plasma spraying are necessary.

The combination of surface engineering strategies (e.g., surface texturing) and coating techniques is a potential solution to obtain high levels of coating properties. Among such techniques, laser surface texturing (LST) stands out because of its noncontact processing, localized treatment area, strong adaptability of processing materials, high

✉ Peng Yi
yipupc@gmail.com

¹ College of Mechanical and Electronic Engineering, China University of Petroleum, No. 66 Changjiang West Road, Huangdao District, Qingdao 266580, China

² School of Mechanical and Control Engineering, Shengli College of China University of Petroleum, Dongying 257061, Shandong, China

flexibility, and environmental protection properties (Ref 13). Studies have proved that laser textures, such as dimples and grooves, can result in reliable mechanical bonding between coatings and substrates (Ref 14, 15). Thus, the application of LST to sprayed coatings has elicited considerable attention (Ref 16, 17). Kromer et al. (Ref 18–21) exerted much effort to explore the effects of laser textures with different texture parameters (e.g., texture volume and diameter/depth ratio) on the adhesion strength of sprayed coatings. They found that LST can be used to enhance coating adhesion and replace the traditional GB. Zinnecker et al. (Ref 22) investigated the effects of femtosecond LST with different pulse lengths, hatch distances, and ablated depths on the interface bond strength between steel and a thermoplastic polymer PA6 film, and found that an optimized tooth-shaped groove texture (GT) can produce a higher lap shear strength than GB. Matějček et al. (Ref 23) studied the effects of LST with different geometric features (e.g., columns and circular holes) on the adhesion of plasma-sprayed W-based coatings in shear loading mode, and revealed significant adhesion improvement over a grit-blasted surface. Xu et al. (Ref 24) studied the influence of single pulse energy and scanning spacing of parallel lines on the coating adhesion of Nb-based boron-doped diamond (BDD) electrodes to provide a new pretreatment method for BDD films, and showed that the adherence properties of BDD films can be improved with the LST pretreatment technique. These existing studies confirmed the effectiveness of LST as a surface pretreatment method in the preparation phase, but most of them focused on dimple textures (DT) and GT. Hence, studies on other texture shapes or the interaction of texture parameters are limited.

To address these issues, Tan et al. (Ref 25) discussed the effects of the interaction between dimple diameter and distance on the coating adhesion of Ni-based sprayed coatings. Their results showed that the interaction of texture parameters exerts an important impact on the adhesion strength improvement of plasma-sprayed coatings. Moreover, the diameter-to-distance ratio was found to be a direct impact factor. Zhang et al. (Ref 26) investigated the effectiveness of multiscale textures on the coating adhesion improvement of PVD TiAlN coatings; in their experimental study, the type of surface texture exerted a profound effect on adhesive strength, and the micro/nanoscale texture was the most effective in improving coating adhesion. In our previous work, we designed a new bionic sinusoidal texture (ST) on the basis of the sinusoidal body structures of a scallop shell (Ref 27); the effects of the bionic STs with and without bulges on the adhesion strength of the plasma-sprayed coatings were analyzed, and the effectiveness of the bionic STs as an alternative to GB was confirmed.

In summary, LST can be used as an effective surface pretreatment technique for coating fabrication because it can improve the coating–substrate adhesion strength. However, the most ideal texture shape has yet to be identified, and a comparative analysis of different texture shapes (e.g., multi-shape–texture) for coating adherence in the case of solid self-lubricating coatings has rarely been reported. Thus, in the present work, we fabricated different textures (DT, GT, ST, and their combination) via LST. Ni-based MoS₂ solid lubricant coatings were deposited on textured surfaces by using the atmosphere plasma spray technique. The effects of the texture shapes on the adhesion properties of the sprayed coatings were identified and discussed. Conventional GB coatings were used for comparison.

Experimental Procedures

Materials

The substrate material was 40Cr steel (0.41 wt% C, 0.35 wt% Si, 0.75 wt% Mn, 1.1 wt% Cr, 0.02 wt% Ni, 0.03 wt% P, 0.03 wt% S, 0.02 wt% Cu, and 97.29 wt% Fe), which is widely used in machinery manufacturing (e.g., gears and shafts). The substrates were machined into buttons with a thickness of 5.1 mm and a diameter of 25.4 mm as per the ASTM 633 standard. Commercial Ni-coated MoS₂ powder (LF235-1; United Coatings Technologies, China) was used, and the particle size ranged from 45 to 106 μm, with the average grain size being 76 μm.

Substrate Surface Preparation

Before LST and GB, the samples were ground using waterproof abrasive papers (600, 800, 1000, 1200, 1500, and 2000 mesh) and polished to a mirror finish with a 1.5-μm diamond polishing agent. The samples were then ultrasonically cleaned for 20 min in alcohol.

Three single-shape textures (DT, GT, and ST) and three multi-shape textures [dimple–groove texture ([DGT), dimple–sinusoidal texture (DST), and sinusoidal–groove texture (SGT)] were designed. The different textures are illustrated in Fig. 1. The design of ST, which can be expressed using Eq. (1), are detailed in Ref. 27 and will not be repeated here.

$$y = A \sin(\omega x + \varphi) + k, \quad (\text{Eq } 1)$$

where A is the amplitude, ω the angular velocity, φ the initial phase, and k the offset distance. A and ω were set to 0.1 and 10, respectively. Given that only A and ω can be

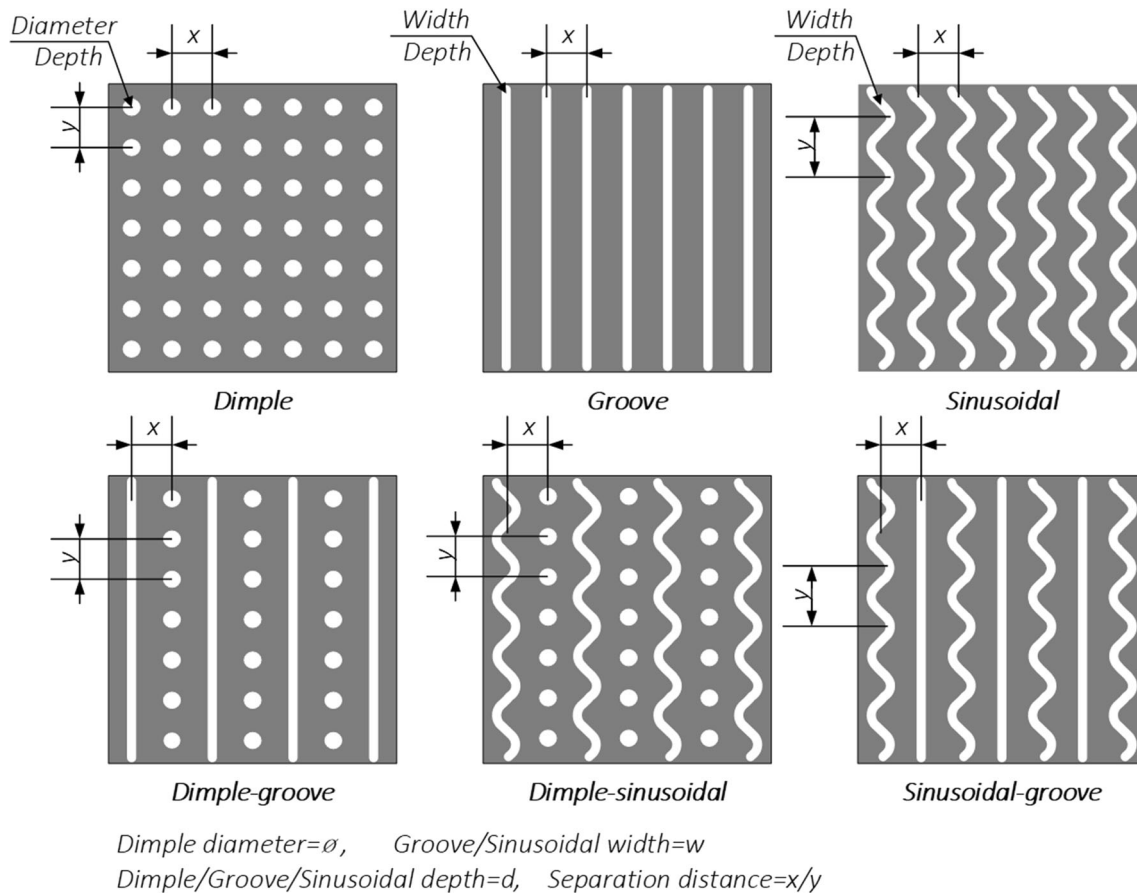


Fig. 1 The different textures

used to control the shape of ST, ϕ and k were set to 0, respectively.

LST was conducted with an IPG laser (YLP-MP20; Han's Laser, China) with a wavelength of 1064 nm and power of 16 W. The pulse duration and repetition rate were 200 ns and 25 kHz, respectively. The scanning with a speed of 400 mm/s was repeated five times and then once to produce ST/GT and DT, respectively. As the dimple dimension influences the filling effect of droplets into cavities, the dimple diameter in this work was set to be slightly larger than the mean particle size (Ref 18). As reported in Ref. 27, coating self-peeling and low adhesion strength usually occur in cases of large texture separation distances (which represent a low texture area ratio). Thus, the texture area ratio was set to 80% and maintained to be constant; it can be expressed using Eq. (2). The dimensions of the textures are listed in Table 1, and were measured with a 3D profilometer (Zeta-20; ZETA Instruments, USA). The average of five textures was used to determine the average texture dimensions, and the actual texture area ratio had a tolerance of 2–5% due to the fast melting and resolidification of the removed materials during the nanosecond laser process. The textured samples were

ultrasonically cleaned for 20 min in alcohol. Samples treated via conventional GB were used for comparison. GB was performed using a pressure-blasting machine with a 40-mesh Al_2O_3 grit at a pressure of 5 bar and distance of 200 mm.

$$R_{\text{area}} = \frac{S_T}{S_0} = \frac{S_{T0}}{x \cdot y} = \frac{w}{x}, \quad (\text{Eq } 2)$$

where R_{area} is the texture area ratio, S_T the total upper surface areas of all the textures, S_0 the area of the substrate, S_{T0} the upper surface area of the texture per unit surface area, w the texture width of GT/ST, and x and y the texture separation distances in the x and y directions, respectively.

Coating Production

Atmospheric plasma spraying was performed to fabricate Ni-based MoS_2 coatings on the laser-textured and grit-blasted substrates. The spraying process was conducted using a TM plasma spraying system with a TM-B torch (both BAMTRI, China). The process parameters are listed in Table 2. The samples were air-cooled during spraying, and the thickness of the obtained coatings was 300 μm .

Table 1 Dimensions of the different textures

Cases	ϕ , μm	w , μm	d , μm	x , μm	y , μm
GB	–	–	–	–	–
ST	–	54.2 + 1.7 – 1.9	25.8 + 1.0 – 0.8	79.0	628
DT	85.2 + 3.4 – 3.3	–	63.7 + 4.1 – 2.8	99.1	99.1
GT	–	53.3 + 1.5 – 1.6	28.5 + 1.6 – 1.3	65.0	–
DGT	85.2 + 3.4 – 3.3	53.3 + 1.5 – 1.6	63.7 + 4.1 – 2.8/28.5 + 1.6 – 1.3	68.4	136.8
DST	85.2 + 3.4 – 3.3	54.2 + 1.7 – 1.9	63.7 + 4.1 – 2.8/25.8 + 1.0 – 0.8	55.2	314.0
SGT	–	54.2 + 1.7 – 1.9/53.3 + 1.5 – 1.6	25.8 + 1.0 – 0.8/28.5 + 1.6 – 1.3	72.0	628

Table 2 Plasma spraying parameters

Parameters	Value
Arc current, A	500
Arc voltage, V	60
Ar gas flow rate, L/min	80
H ₂ gas flow rate, L/min	10
Powder feed rate, g/min	28
Spraying distance, mm	100

Characterization Methods

The topography of the laser-textured surfaces was observed with the above 3D profilometer. The cross-section and fractured surface of the coatings were characterized via scanning electron microscopy (SEM) (JSM-7200F; JEOL, Japan). Energy-dispersive x-ray spectroscopy (EDS) (X-Max50; Oxford, UK) was performed to study the element distribution of the coating–substrate and fracture interfaces. The phase composition of each coating was investigated with an X-ray diffractometer (XRD-6100B; SHIMADZU, Japan) with CuK α radiation in steps of 0.02°. The cross sections of the coated samples were ground, polished, and ultrasonically cleaned before observation.

The adhesion strength of the coatings was investigated using a universal test machine (3369; INSTRON, USA) with an applied load rate of 1.27 mm/min in accordance with the ASTM 633 standard. Before the pull-off test, the uncoated surfaces of the test buttons and one surface of the connecting blocks were grit-blasted, and the test buttons were bonded to two blocks by using FM1000 epoxy (Fig. 2). The jointed specimens were placed in a furnace at 180 °C with a holding time of 180 min. The average of the three tests was used to determine the adhesion strength.

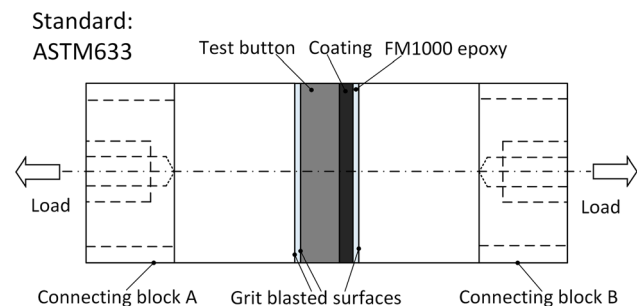


Fig. 2 Schematic of the pull-off test of plasma-sprayed coatings

Results

Morphology of Substrate Surfaces

The topography of the textures with different shapes is shown in Fig. 3. Bulges, which differ according to texture shape and are formed by the accumulation of molten metal ejected from the ablation pit during laser processing, were observed on the edges of all the textures. Figure 3(a), (c), (e) shows that the bulge surrounding DT was wider than those surrounding ST and GT. This result is attributed to the production of DT via spiral scanning in contrast to the production of ST and GT via linear scanning. Furthermore, all the textures were produced by multiple laser pulses; thus, the 2D cross-section profiles of the textures fluctuated during measurement, as shown in Fig. 3(b), (d), (f). Surface contamination (possibly metal oxides), which influences the bond quality of coatings (Ref 28, 29), was observed on the untextured surface between the textures because laser texturing belongs to thermal processing. The so-called contamination was formed by the vapor deposition with plasma during laser processing. Moreover, Ref. 27 indicated that texture bulges significantly affect the adhesion strength of the sprayed coatings by causing fractures within the coating rather than at the coating–substrate interface for textured surfaces with bulges. If all the coatings are fractured within the coating in the adhesion test, then the results cannot reflect the influence of texture

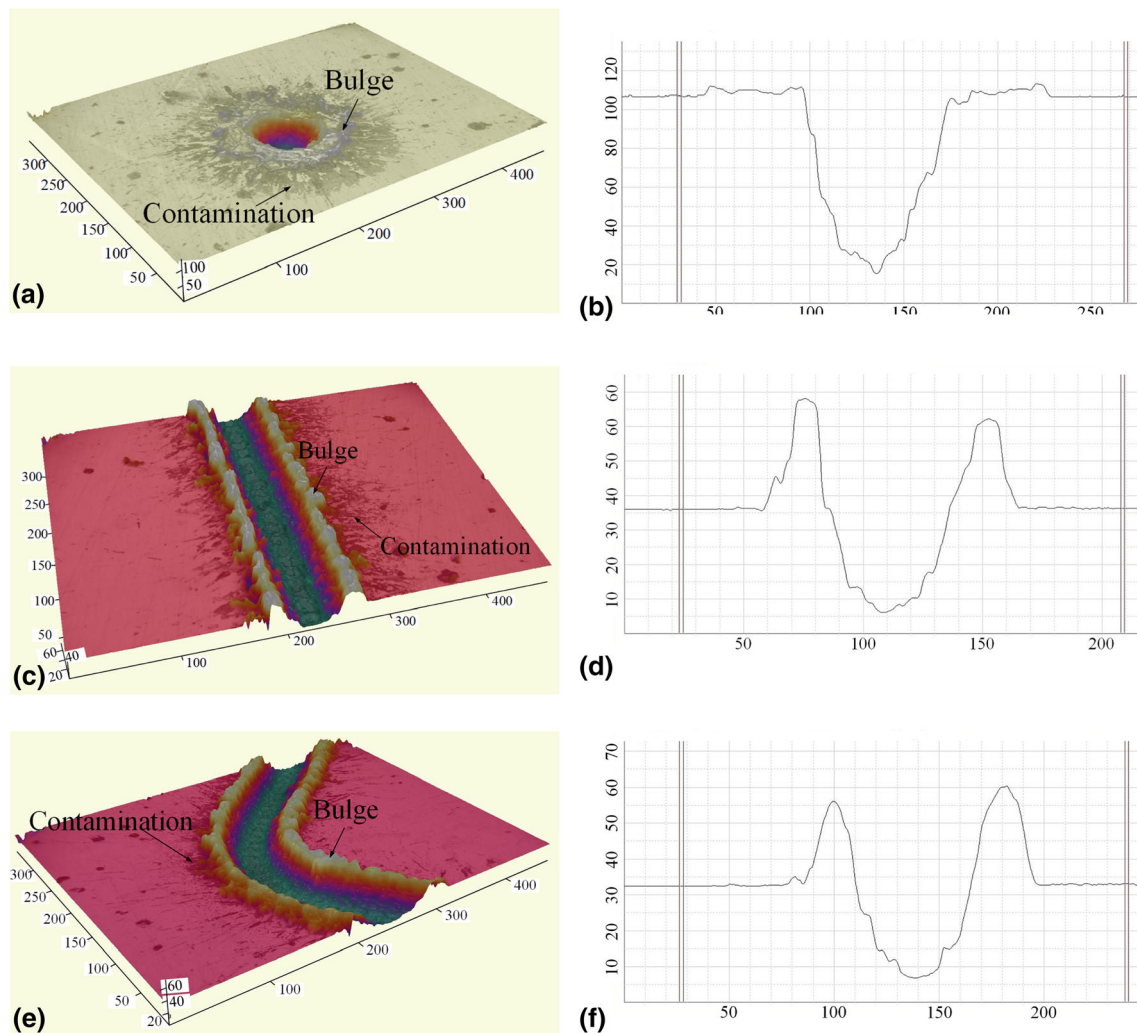


Fig. 3 Morphology of different textures: (a), (c), and (e) the 3D topographies of DT, GT, and ST, respectively; (b), (d), and (f) the 2D cross-section profiles of DT, GT, and ST, respectively

shapes on bond strength. In such a case, we cannot determine which shape is ideal. Therefore, in the current work, the textured surfaces were polished and ultrasonically cleaned before plasma spraying to remove the bulges and contaminations. As smooth regions adversely affect coating adhesion (Ref 27), we could use the characteristic of smooth regions to fracture the coating from the interface and thereby facilitate this work. The SEM images of the textured surfaces before and after polishing (Fig. 4) show that, after polishing, the bulges and contaminations around the textures were removed and that the surface between the textures became clean and smooth. When the separation distances of the textures varied, only the area of the untextured surface between the textures changed. Moreover, the multi-shaped textured surfaces contained all the texture shapes. Therefore, the DT, GT, and ST surfaces are not repeated here.

Deposition Characteristics of Coatings

Deposition Characteristics of Grit-Blasted Coatings

The microstructure of the plasma-sprayed coating based on SEM in backscattered mode is presented in Fig. 5. The coating exhibits a lamellar structure and rough surface. It also shows pores, cracks, and partially melted particles, all of which are commonly observed in plasma-sprayed coatings and are difficult to eliminate completely. The pores probably resulted from the imperfect overlapping of the splats or gaps within the agglomerated powders (Ref 30, 31). The substrate surface is wavy, rough, and suitable for the bonding of the coating to the substrate. However, several defects produced by GB can be observed on the substrate surface (Fig. 5b). These defects may adversely affect the adhesion properties of the coating

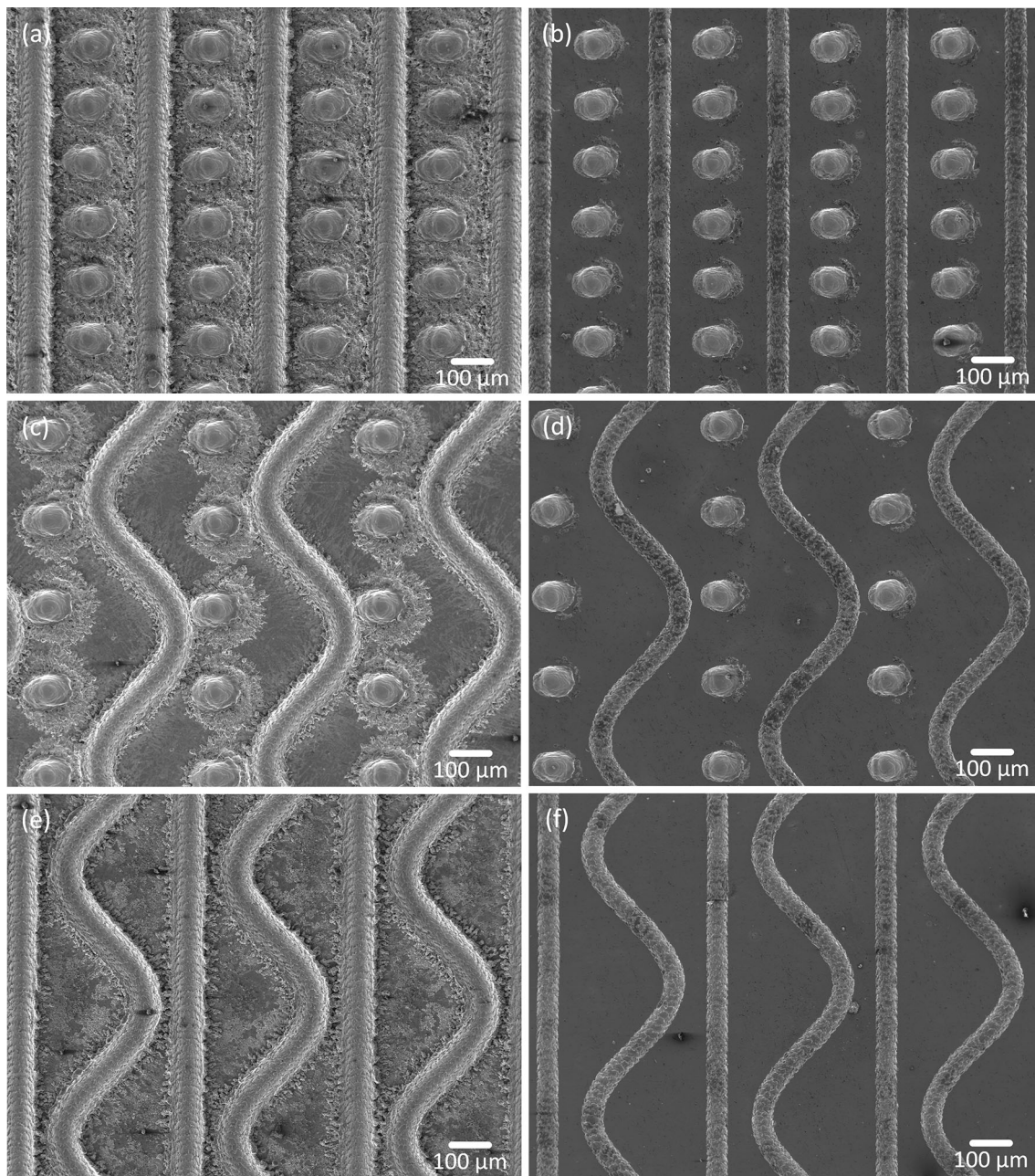


Fig. 4 SEM images of textured surfaces: (a), (c), and (e) the unpolished surfaces of DGT, DST, and SGT, respectively; (b), (d), and (f) the polished surfaces of DGT, DST, and SGT, respectively

because a large gap can be produced between the coating and the substrate near the defects.

Figure 6 shows the x-ray diffraction (XRD) pattern of the sprayed coating. Ni_xS_y , such as NiS, Ni_3S_2 , and NiSO_4 , was formed during spraying, thereby indicating that the chemical reaction between Ni and MoS_2 occurred at a high temperature. The formation of NiO and Mo_xO_y , such as MoO_3 and Mo_4O_{11} , revealed that oxidation occurred during spraying. Several of these oxides, such as NiO, MoO, and Mo_4O_{11} , can be used as high-temperature solid

lubricants (Ref 32, 33). Furthermore, the MoS_2 phase peak was not observed in the XRD pattern. However, the distribution of elements in Fig. 5(b) suggests that several MoS_2 phases, such as the white phases marked by dashed lines, were retained in the coating. This result may be explained as follows: although MoS_2 was coated with a Ni protective layer, the dispersive distribution of S and Mo in the coating (Fig. 7) further indicated that MoS_2 was decomposed during spraying and reacted with other substances (Fig. 6). Thus, the MoS_2 content decreased in the

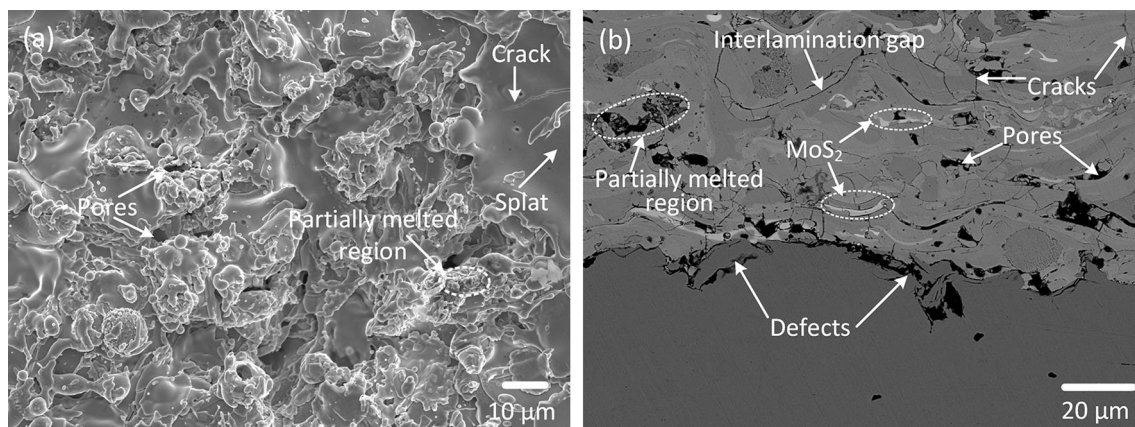


Fig. 5 Microstructure of the sprayed coating on the grit-blasted surface

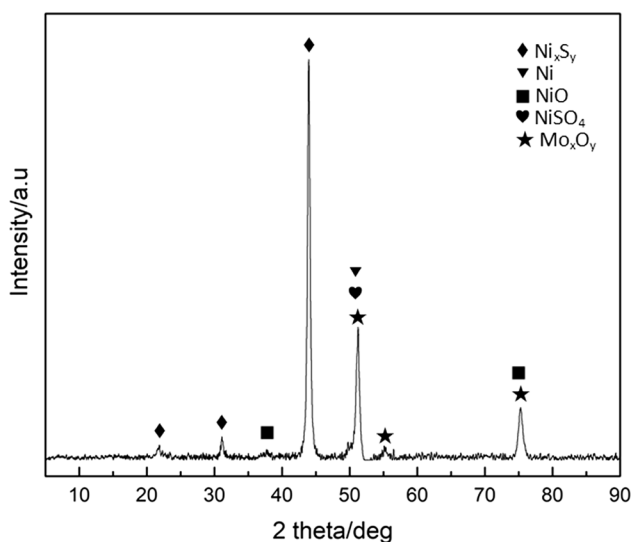


Fig. 6 XRD pattern of the sprayed coating

coating, resulting in the possible absence of MoS_2 in the XRD range.

Deposition Characteristics of Coatings on Textured Surfaces

Figure 8 presents the cross-sectional images of the plasma-sprayed coatings with DGT, DST, and GST. The cross-sectional images of the plasma-sprayed coatings on the DT, GT, and ST surfaces are not shown in the figure because the filling state of the sprayed droplets in the textures was unaffected by the adjacent textures, and the single-shape textured surfaces were covered by multi-shape textured surfaces. Furthermore, the specimens were round; thus, accurately determining the direction of GT and ST and the position of DT is difficult after the textured surfaces are coated. Ensuring that the cross-sections are perpendicular to the linear texture (GT and ST) and are passing through

the middle of DT is also challenging. Hence, the texture dimensions, such as width, depth, and width of a plain area visible on the cross-sections, were different from the set values.

The microscopic analysis of the coatings revealed pores and cracks in the coatings of the textured samples, especially in the DT regions. A good bond state was observed in the GT/ST positions. Figure 8(b) and (d) shows the incomplete filling and interface gap inside DT; such a phenomenon was not accidental. Ref. 17, 18, and 34 also reported similar phenomena. Further studies are needed to verify whether these defects can be eliminated by adjusting the spraying parameters, powder parameters, or texture parameters. Given that the inner wall of DT is closed, air is trapped at the bottom when a molten particle penetrates a dimple. When the volume of the trapped air is compressed, the pressure increases, and an interface gap is generated between the droplet and the inner wall of DT. For GT and ST, air can escape along the longitudinal direction of the texture. Thus, the contact state between the droplets and the inner wall of the textures improves. When a large droplet formed by large or agglomerated particles that are larger than the dimple diameter penetrates a dimple, the dimple is completely covered, the movement of the droplet is limited by the texture wall and trapped air, and incomplete filling is likely to occur.

In the region where the width of the plain area is small enough, the resolidified molten metal (sputtered from the adjacent texture) can be observed in the texture, as shown in Fig. 8(f). This resolidified molten metal results in a shallow texture depth and enlarges the plain area, but it also creates new holding-on areas within the texture. In this work, the samples were ultrasonically cleaned for 20 min in alcohol before and after laser texturing. Then, some resolidified molten metal particles with poor adhesion were removed because the alcohol became turbid after the textured samples were ultrasonically cleaned. Furthermore,

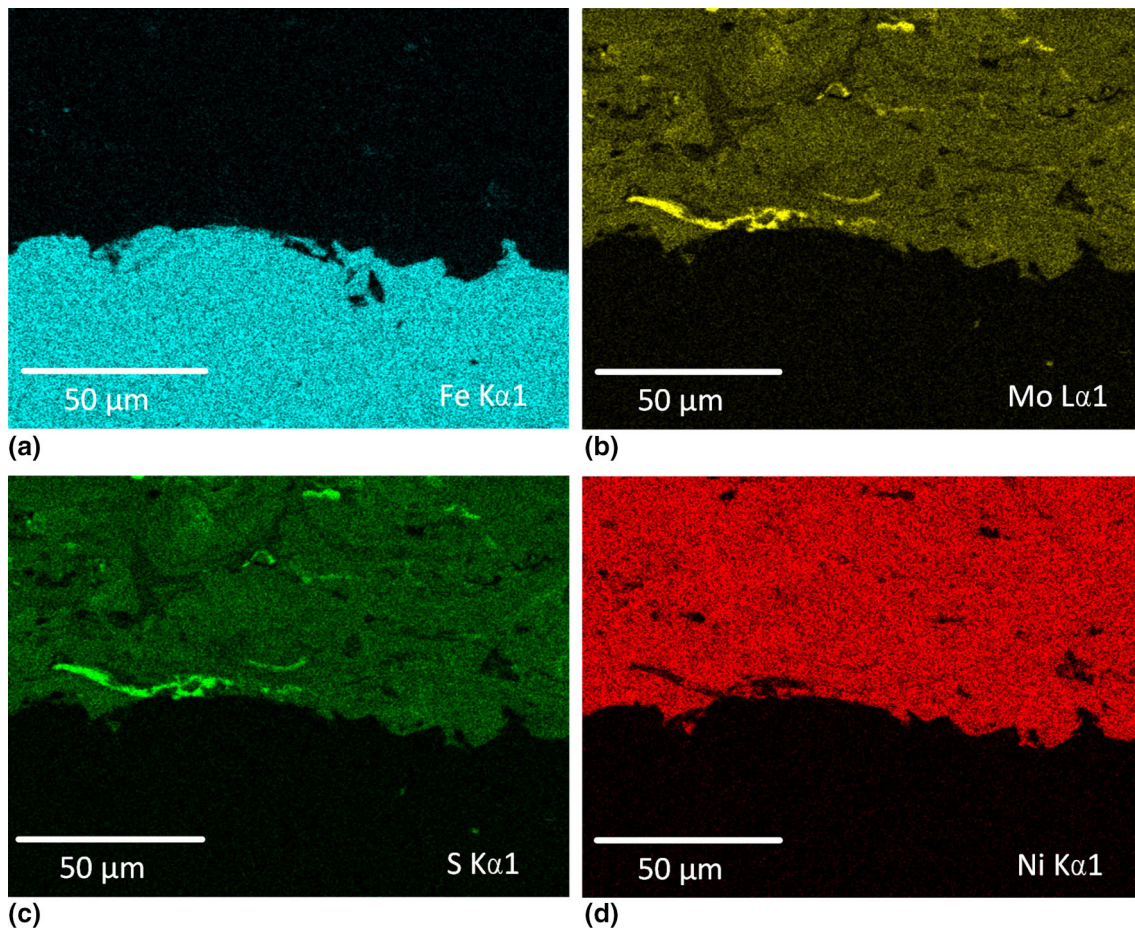


Fig. 7 Element distribution in the cross-section of the grit-blasted and coated samples

Fig. 8(f) shows a metallurgical bond between the resolidified molten metal and the texture wall; however, such a result is reliable. Particles that appear to be separated from the substrate may be a part of the resolidified molten metal connected to the substrate; otherwise, it is removed during ultrasonic cleaning. Therefore, we inferred that these resolidified molten metals benefited the coating adhesion. Further studies are needed to determine the existence of weakly bound resolidified molten metal particles, which might undermine coating adhesion.

Adhesion Strength Improvement and Fracture Morphology

Figure 9 shows the results of the adhesion strength test. The average adhesion strength of the coating on the GT and ST surfaces was higher than that of the coating on the grit-blasted surface (41.3 MPa), and the samples of ST attained the highest adhesion strength of 50.0 MPa. DGT exhibits the lowest adhesion strength of 21.8 MPa, followed by DT (27.0 MPa). The adhesion strength of the coatings on all the multi-shape textured surfaces was lower than those of

the coatings on the GT and ST surfaces. Adhesion strength might have been affected by the interaction between the different texture shapes, as discussed later. The above analysis indicates that ST could be the best alternative to GB prior to plasma spraying to improve the adhesion strength of coatings.

Figure 10 shows the fracture morphologies of the coating on the grit-blasted specimen after the pull-off test. As coating materials remained on the substrate (Fig. 10a), the fracture type of the coating on the grit-blasted surface belonged to a typical mixed mode at the substrate/coating interface and within the coating; this fracture type corresponded to adhesive and cohesive failures, respectively (Ref 35). Figure 10(b) shows the microstructure and EDS results of the fractured surface (inset in Fig. 10b) captured from area A in Fig. 10(a). Fe (which was not present in the coating) was detected, thereby further confirming the mixed failure in the grit-blasted coating.

Figure 11 presents the macroscopic fractured surfaces of the specimens with different texture shapes after the pull-off test. The adhesive failure mode that occurred at the substrate/coating interface played a key role in coating DT,

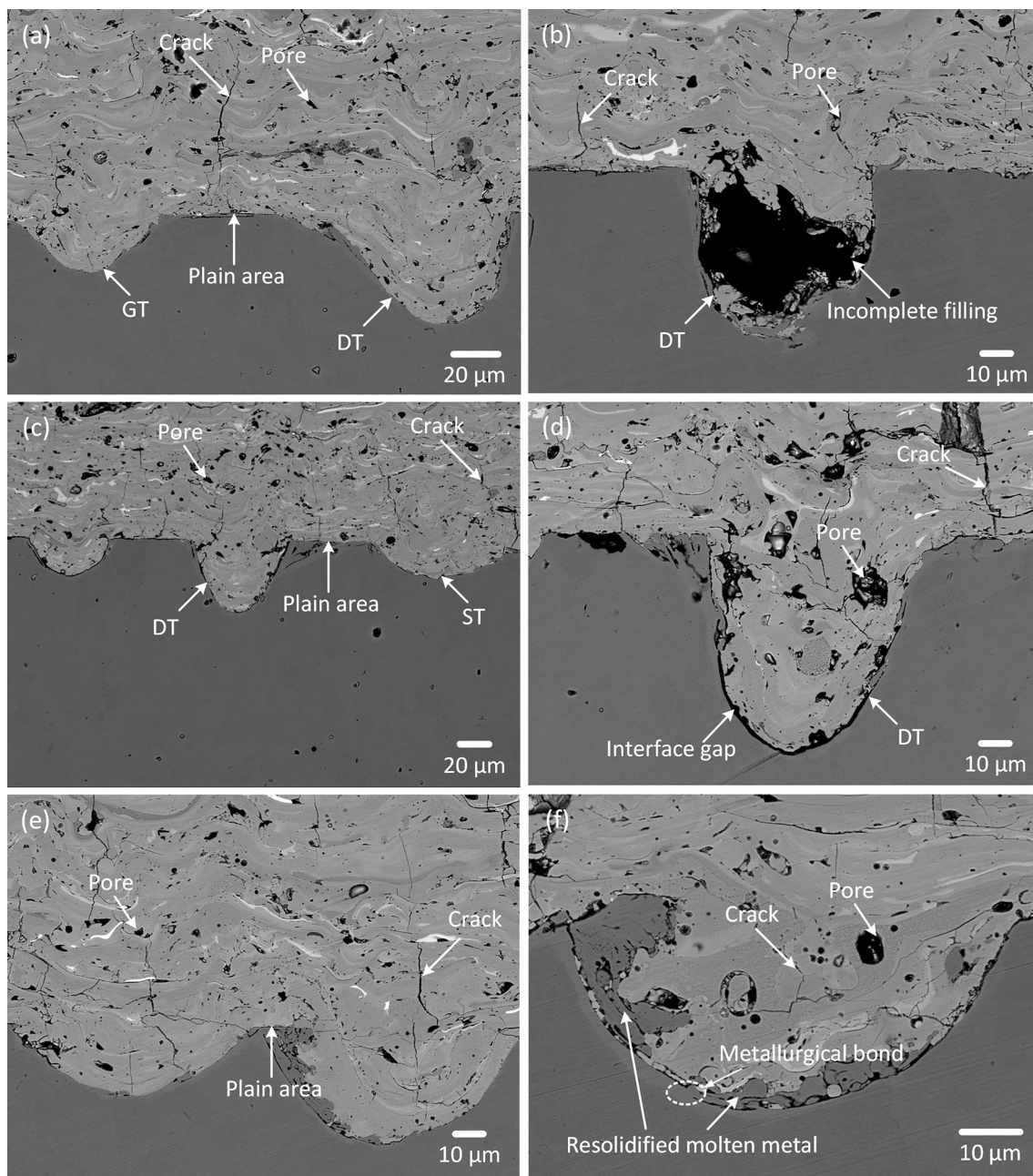


Fig. 8 Cross-sectional image of plasma-sprayed coatings with different texture shapes: (a, b) DGT, (c, d) DST, and (e, f) SGT

DGT, DST, and SGT because the coating material could hardly be observed on the fractured surfaces; only a small amount of coating material was noted in the case of DST and SGT. An obvious coating material residue was observed in the specimens of GT and ST, which indicated a mixed failure mode and high adhesion strength. The failure began at the substrate/coating interface and expanded to the interior of the coating. Macroscopic analysis indicated that multi-shape textures are not conducive to the improvement of coating adhesion.

Discussion

Micromorphology Analysis of Fractured Surfaces

The SEM micrographs of the fractured surfaces obtained from the samples in Fig. 11 are shown in Fig. 12 to further understand the fracture mechanism of the coatings on the textured surfaces. Reports showed that five mechanical bond styles, namely, embedding, anchoring, holding on, spreading, and a combination of the four, contribute to the mechanical bond of sprayed coatings, with spreading and

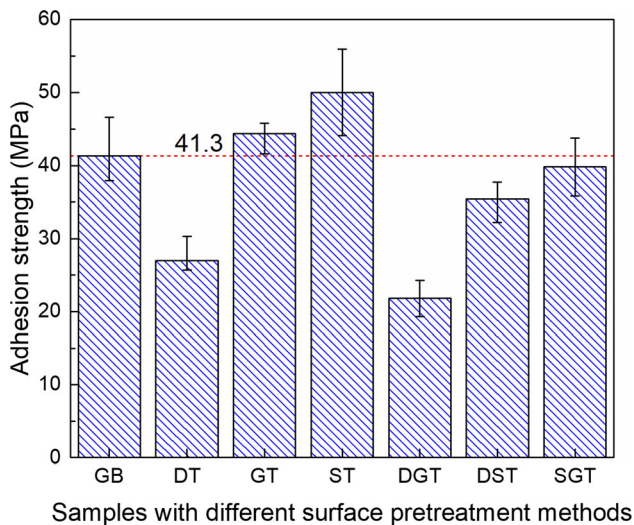


Fig. 9 Adhesion strength of sprayed coatings with different texture shapes

holding-on being the weakest and strongest bond styles, respectively (Ref 25, 27). Almost all of the textures were covered by the coating materials for ST, and only a few plain areas were visible (Fig. 12c). Thus, the failure mode in the ST samples was mainly cohesive failure, while slight adhesive failure occurred in several plain areas, leading to the high adhesion strength. For DT and GT, almost all the plain areas were visible because the molten particles typically formed a weak bond (spreading bond) on the smooth surfaces. The coatings were embedded in the textures, and several coating materials were observed in the textures in Fig. 12(a) and (b). This result indicated that the microfracture mechanism of DT and GT was mixed failure (adhesive failure + cohesive failure). Figure 12(a) shows that the coatings in the textured areas were mainly fractured inside the dimples (e.g., D1). Moreover, the coatings fractured from the upper surface of the dimples (e.g., D2 and D3) were observed in only a few textured areas. Figure 8 indicates that incomplete filling and pores were easily produced in the dimples and that cracks formed around the

Fig. 10 Fractographs of the grit-blasted specimen

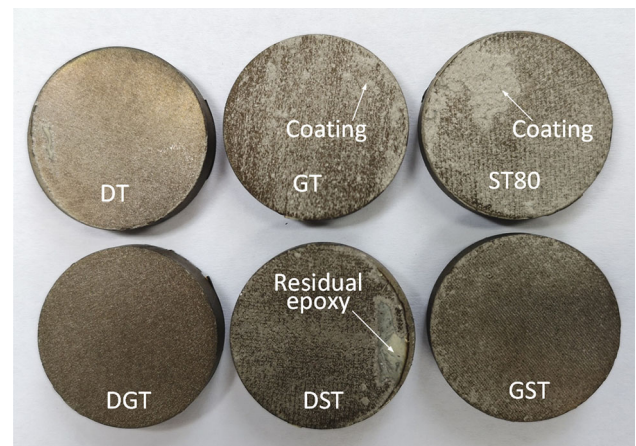
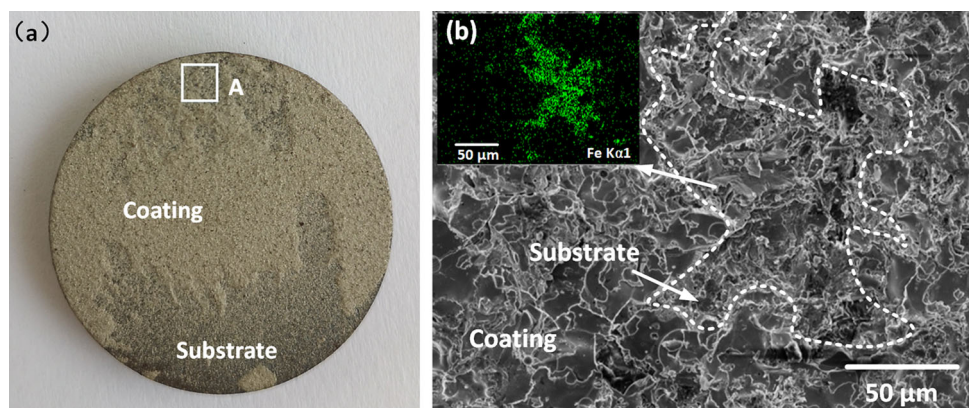


Fig. 11 Fractured surfaces of coatings with different texture shapes after pull-off tests

pores. These defects reduced the cohesive strength of the coatings in the dimples and caused the coatings to easily fracture from such defects. As shown in Fig. 13, the inner wall of a dimple was remarkably smooth and thus hindered the adhesion of the molten particles to the dimple. This phenomenon may also explain the interface gap in the dimple in Fig. 8(d). The adhesive strength between the coating and the inner wall of DT decreased. However, sputtering morphology, which was caused by the recoil of laser pulses, was observed inside GT and ST. Sputtering morphology can roughen the inner walls of these textures and act as holding-on structures for molten particles, leading to a good bonding state. These factors would eventually lead to the adhesion strength of DT being lower than that of GT and ST.

If DT is combined with GT/ST, then DT restrains the adhesion strength enhancement effect of the other textures. As shown in the fractured surfaces of DGT and DST (Fig. 12(d) and (e), respectively), the coating was almost completely peeled off from the dimples, whereas it fractured within the coating at the GT/ST positions, with the coating materials remaining in GT/ST. Under the effect of

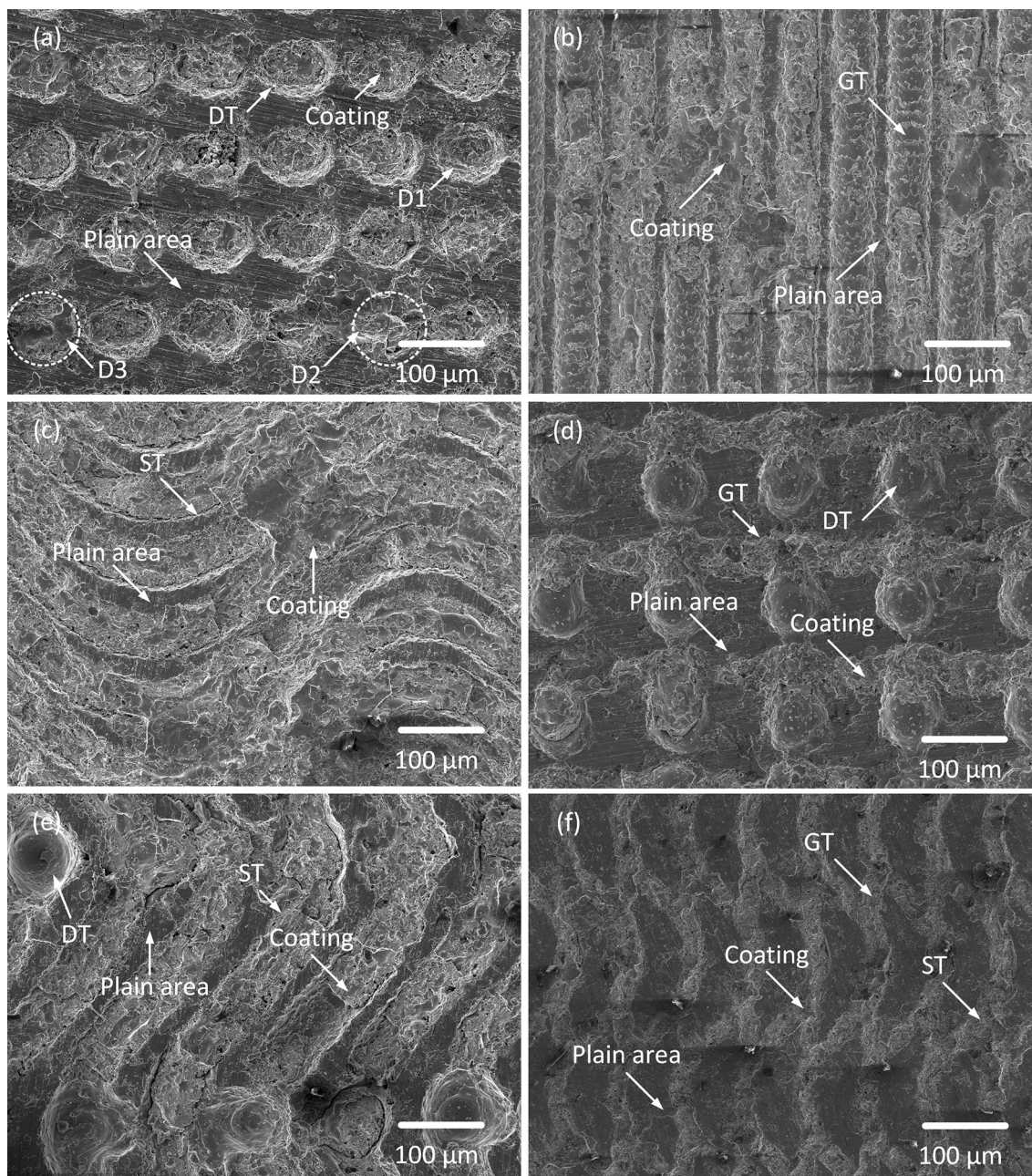


Fig. 12 SEM fractographs of the fractured surfaces with different texture shapes: (a) DT, (b) GT, (c) ST, (d) DGT, (e) DST, and (f) SGT

DT, the microfracture mechanism of DGT/DST was cohesive failure in the GT/ST regions and adhesive failure in the DT and plain areas. When GT was combined with ST (Fig. 12f), all of the textures were covered with the coating materials, but the substrate was completely exposed in the plain area. Hence, the fracture mode became adhesive failure in the plain area regions and cohesive failure in the textures. Figure 9 shows that the adhesion strength of SGT was lower than that of GT/ST. Although GT and ST improved the coating adhesion, their combination did not produce beneficial results possibly because

crescent-like plain regions were created when GT was combined with ST (Fig. 12f). These crescent-like plain regions were much wider than the narrow plain areas in GT/ST. In general, a narrow plain area helps to reduce the spreading bond effect, whereas a wide crescent-like plain area provides enough space for molten particles to spread, thereby decreasing the coating adhesion.

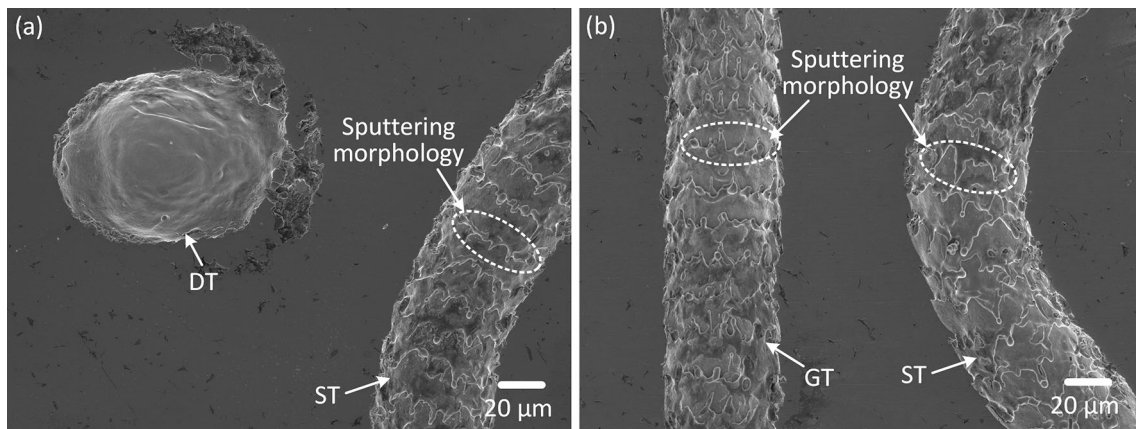


Fig. 13 Microstructure of different texture shapes

Contact Area Ratio Between Coating and Substrate

In addition to the bond style, the contact area ratio, which represents the ratio of the contact between the coating and the substrate, is another important factor influencing adhesion strength due to the mechanical anchoring mechanism of the sprayed coatings (Ref 17, 25). The contact area ratio is defined by Eq. (3), and the interface area (red line in Fig. 14) was computed using ImageJ software.

$$R_{con} = \frac{A_{Pre}}{A_{Pla}}, \tag{Eq 3}$$

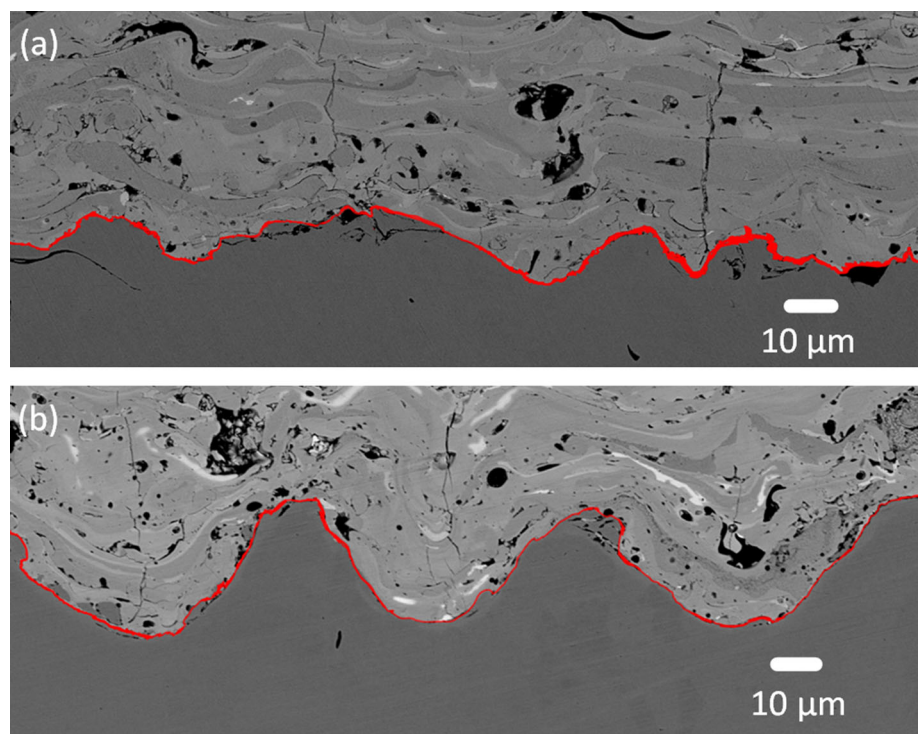
where R_{con} is the contact area ratio, A_{Pre} the interface area of the pretreated surface (grit blasted or laser textured), and

A_{Pla} the area of the planar surface. However, in Ref. 17, only the contact area of a single texture was calculated, and the effect of texture separation distance was not considered. R_{area} is introduced into Eq. (3), and then Eq. (3) is changed to Eq. (4):

$$R_{con} = \frac{A_{Pre}}{A_{Pla}} = \frac{A_{Tes} + (1 - R_{area})A_{Pla}}{A_{Pla}} = \frac{A_{Tes}}{A_{Pla}} + (1 - R_{area}), \tag{Eq 4}$$

where A_{Tes} is the sum of the inner surface areas of all textures in the calculated region. According to Eqs. (3) and (4), the contact area ratio is directly related to the texture separation distance. Adhesion strength can then be

Fig. 14 The interface area: (a) grit-blasted surface and (b) laser-textured surface



theoretically predicted using Eq. (5) (Ref 19) and is definitely linked to texture separation distance:

$$F = \bar{\mu} \bar{P} R_{\text{con}}, \quad (\text{Eq 5})$$

where F is the adhesion strength, $\bar{\mu}$ the average friction coefficient, and \bar{P} the average pressure.

Therefore, adhesion strength has been shown to be linearly linked to R_{con} . Figure 15 presents the contact area ratios for different surface pretreatments. The analysis showed that DT had the most significant effect on the R_{con} of the textured surface and that the combination of DT and other textures could increase R_{con} . In general, increasing R_{con} provides more embedding areas, fewer spreading areas, and more uneven obstacles for melted particles, all of which increase the energy necessary for crack propagation; hence, an increasing adhesion strength of sprayed coatings was expected here (Ref 19). However, DT and its multi-shape textures had relatively low adhesion strength (Fig. 9). This result indicated that the unfavorable factors

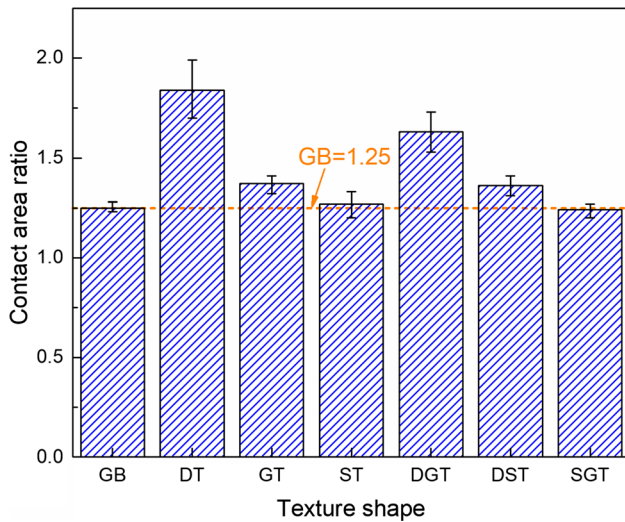


Fig. 15 Contact area ratios for surfaces with different texture shapes

of the DT coating, rather than R_{con} , play a dominant role in coating adhesion. The detrimental effect of DT on adhesion strength enhancement was further demonstrated. Although some optimization work of DT has been carried out in Ref. 18 and 25, the bond strength of the coatings on the optimized dimple-textured surfaces is still lower than that of the ST under similar DT contact area ratio conditions. SGT had a similar R_{con} to ST, but the adhesion strength of SGT was 20% lower than that of ST. This result further confirmed the adverse effect of crescent-like plain regions (which promote spreading bonds) on adhesion strength improvement. Furthermore, the reasons for the difference in the adhesion strength of ST and GT need to be further studied. Nevertheless, the effectiveness of ST in improving the adhesion strength of plasma-sprayed coatings can be confirmed in the current work. In sum, factors such as coating bond style, contact area ratio, and coating deposition quality should be comprehensively considered in texture design to improve coating adhesion.

The above analysis indicates that texture shape has a significant effect on adhesion strength improvement. Under the experimental conditions in this work, ST proved to be the best choice for improving adhesion strength, followed by GT, while DT had the worst effect. Combining different textures did not produce beneficial effects. In the GT or ST regions, the coating usually fractured at the top surface of the textures, as shown in Fig. 16(a). In the DT regions (Fig. 16b), the interface gap between the coating and the inner wall of DT caused the coating to completely peel off from the dimples. The coating on the DT regions can also be fractured by these defects because incomplete filling and large pores easily form inside dimples and cracks usually occur around pores. Furthermore, coating debonding from the upper surface of textures may occur in a few DT regions, as marked by the dotted line in Fig. 16(b). In the plain areas, the coatings easily fractured from the coating/substrate interface, thus indicating that the existence of a plain area may be harmful to the improvement of coating

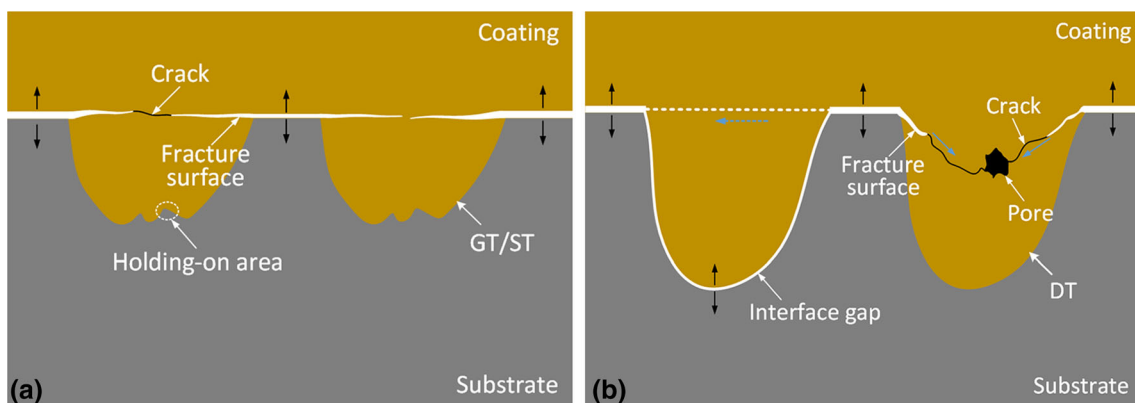


Fig. 16 Schematic of the coating fracture mechanism: (a) coatings with GT/ST and (b) coatings with DT

adhesion. Although we made extensive efforts to investigate the effects of texture shapes on the adhesion strength properties of sprayed coatings, further studies are still necessary, particularly with regard to other analysis methods, texture parameters, surface roughness, and wettability.

Conclusions

The effects of texture shape (dimple texture, groove texture, sinusoidal texture, and their combination) on the adhesion properties of plasma-sprayed coatings have been investigated. The macro- and microfracture characteristics of the coatings have been analyzed. The main conclusions are:

1. Ni-based MoS₂ self-lubricating coatings with a typical lamellar structure were fabricated via plasma spraying. The existence of Ni_xS_y, NiO, and Mo_xO_y indicated the occurrence of oxidation and a chemical reaction between Ni and MoS₂ during spraying, resulting in a decreased MoS₂ content.
2. The bond state of the sprayed coatings varied with the texture shape. A good contact state was obtained in the groove/sinusoidal texture positions, and incomplete filling and an interface gap were observed in the dimple textures. Under the given conditions, the sinusoidal texture had the highest adhesion strength of 50.0 MPa, followed by the groove texture, whose adhesion strength was higher than that of grit-blasting (41.3 MPa); the dimple texture and dimple–groove texture had the lowest adhesion strength. The adhesion strength of the coatings on all the multi-shape textured surfaces was lower than those of the coatings on the groove-textured and sinusoidal-textured surfaces. These results indicate that the sinusoidal texture is the ideal choice to improve the adhesion strength. The compounding of different textures was found to be unhelpful.
3. The fracture morphology analysis revealed that cohesive failure was dominant for sinusoidal-textured samples because almost all of the textures were covered by the coating materials. Mixed failure occurred for the other texture shapes, and adhesive failure easily occurred in dimple textures and in almost all of the plain areas. This result suggests that plain areas and dimple textures may restrain adhesion strength enhancement. Factors such as coating bond style, contact area ratio, and coating deposition quality should be comprehensively considered in texture design to improve coating adhesion.

Acknowledgments This study was supported by the Shandong Provincial Natural Science Foundation (No. ZR2019MEE043), the Petro China Innovation Foundation (No. 2017D-5007-0307), and the Fundamental Research Funds for Central Universities (No. 18CX02086A).

References

1. L. Rapoport, A. Moshkovich, V. Perilyev, A. Gedanken, Y. Kolytyn, E. Sominski, G. Halperin, and I. Etsion, Wear Life and Adhesion of Solid Lubricant Films on Laser-Textured Steel Surfaces, *Wear*, 2009, **267**(2), p 1203-1207
2. S. Chatterjee, J.D. Majumdar, S.M. Shariff, G. Padmanabham, and A.R. Choudhury, Effect of Laser Post-treatment on Al₂O₃-TiB₂-TiN Composite Coating with Free hBN, *Int. J. Adv. Manuf. Technol.*, 2012, **61**(5), p 559-567
3. F. Akhlaghi and S. Mahdavi, Effect of the SiC Content on the Tribological Properties of Hybrid Al/Gr/SiC Composites Processed by In Situ Powder Metallurgy (IPM) Method, *Adv. Mater. Res.*, 2011, **264**, p 1878-1886
4. H. Algul, M. Tokur, S. Ozcan, M. Uysal, T. Cetinkaya, H. Akbulut, and A. Alp, The Effect of Graphene Content and Sliding Speed on the Wear Mechanism of Nickel-Graphene Nanocomposites, *Appl. Surf. Sci.*, 2015, **359**, p 340-348
5. S. Wu, S. Tian, P.L. Menezes, and G. Xiong, Carbon Solid Lubricants: Role of Different Dimensions, *Int. J. Adv. Manuf. Technol.*, 2020, **107**, p 3875-3895
6. H. Yi, L. Qi, J. Luo, Y. Guo, S. Li, and N. Li, Elimination of Droplet Rebound Off Soluble Substrate in Metal Droplet Deposition, *Mater. Lett.*, 2018, **216**, p 232-235
7. M. Naebe and K. Shirvanimoghaddam, Functionally Graded Materials: A Review of Fabrication and Properties, *Appl. Mater. Today*, 2016, **5**, p 223-245
8. W. Xiong and P. Cheng, Mesoscale Simulation of a Molten Droplet Impacting and Solidifying on a Cold Rough Substrate, *Int. Commun. Heat Mass*, 2018, **98**, p 248-257
9. H.B. Parizi, J. Mostaghimi, L. Pershin, and H.S. Jazi, Analysis of the Microstructure of Thermal Spray Coatings: A Modeling Approach, *J. Therm. Spray Technol.*, 2010, **20**(19), p 736-744
10. V. Pershin, M. Lufitha, S. Chandra, and J. Mostaghimi, Effect of Substrate Temperature on Adhesion Strength of Plasma-Sprayed Nickel Coatings, *J. Therm. Spray Technol.*, 2003, **12**(3), p 370-376
11. C. Coddet, G. Montavon, S. Ayrault-Costil, O. Freneaux, F. Rigolet, G. Barbezat, F. Folio, A. Diard, and P. Wazen, Surface Preparation and Thermal Spray in a Single Step: The PROTAL Process—Example of Application for an Aluminum-Base Substrate, *J. Therm. Spray Technol.*, 1999, **8**(2), p 235-242
12. P. Fauchais, A. Vardelle, M. Vardelle, and M. Fukumoto, Knowledge Concerning Splat Formation: AN Invited Review, *J. Therm. Spray Technol.*, 2004, **13**(3), p 337-360
13. X. Wang, J. Duan, M. Jiang, S. Ke, B. Wu, and X. Zeng, Study of Laser Precision Ablating Texture Patterns on Large-Scale Free-form Surface, *Int. J. Adv. Manuf. Technol.*, 2017, **92**(9), p 4571-4581
14. A. Lamraoui, S. Costil, C. Langlade, and C. Coddet, Laser Surface Texturing (LST) Treatment Before Thermal Spraying: A New Process to Improve the Substrate-Coating Adherence, *Surf. Coat. Technol.*, 2010, **205**, p S164-S167
15. Y. Li, Y. Guan, Z. Zhang, and S. Ynag, Enhanced Bond Strength for Micro-Arc Oxidation Coating on Magnesium Alloy via Laser Surface Microstructuring, *Appl. Surf. Sci.*, 2019, **478**, p 866-871
16. R. Viana, M.S.F. de Lima, W.F. Sales, W.M. Da Silva, and A.R. Machado, Laser Texturing of Substrate of Coated Tools—

- Performance during Machining and in Adhesion Tests, *Surf. Coat. Technol.*, 2015, **276**, p 485-501
17. R. Kromer, S. Costil, J. Cormier, D. Courapied, L. Berthe, P. Peyre, and M. Boustie, Laser Surface Patterning to Enhance Adhesion of Plasma Sprayed Coatings, *Surf. Coat. Technol.*, 2015, **2015**(278), p 171-182
 18. R. Kromer, J. Cormier, and S. Costil, Role of Powder Granulometry and Substrate Topography in Adhesion Strength of Thermal Spray Coatings, *J. Therm. Spray Technol.*, 2016, **25**(5), p 933-945
 19. R. Kromer, S. Costil, J. Cormier, L. Berthe, P. Peyre, and D. Courapied, Laser Patterning Pretreatment before Thermal Spraying: A Technique to Adapt and Control the Surface Topography to Thermomechanical Loading and Materials, *J. Therm. Spray Technol.*, 2016, **25**(3), p 401-410
 20. R. Kromer, Y. Danlos, E. Aubignat, C. Verdy, and S. Costil, Coating Deposition and Adhesion Enhancements by Laser Surface Texturing-Metallic Particles on Different Classes of Substrates in Cold Spraying Process, *Mater. Manuf. Process.*, 2017, **32**(14), p 1642-1652
 21. R. Kromer, S. Costil, C. Verdy, S. Gojon, and H. Liao, Laser Surface Texturing to Enhance Adhesion Bond Strength of Spray Coatings-Cold Spraying, Wire-Arc Spraying, and Atmospheric Plasma Spraying, *Surf. Coat. Technol.*, 2018, **352**, p 642-653
 22. V. Zinnecker, C. Stokesgriffin, S. Madden, A. Rode, and P. Compston, Investigation of the Effects of Femtosecond Laser Metal Surface Texturing on Bonding of PA 6 to Steel, *Procedia Manuf.*, 2019, **29**, p 313-320
 23. J. Matějčicek, M. Vilemova, D. Moskal, R. Musalek, J. Krofta, M. Janata, Z. Kutílek, J. Klečka, S. Heuer, J. Martan, E. Nardoza, Š. Houdková, and D. Dorowgerspach, The Role of Laser Texturing in Improving the Adhesion of Plasma Sprayed Tungsten Coatings, *J. Therm. Spray Technol.*, 2019, **28**(7), p 1346-1362
 24. C. Xu, F. Xu, L. Shi, J. Gao, L. Tu, and D. Zuo, Enhancement of Substrate-Coating Adherence of Boron-Doped Diamond Electrodes by Nanosecond Laser Surface Texturing Pretreatment, *Surf. Coat. Technol.*, 2019, **360**, p 196-204
 25. N. Tan, Z. Xing, X. Wang, H. Wang, G. Jin, S. Chen, and B. Xu, Deposition Mechanism of Plasma Sprayed Droplets on Textured Surfaces with Different Diameter-to-Distance Ratios, *Mater. Des.*, 2017, **133**, p 19-29
 26. K. Zhang, J. Deng, X. Guo, L. Sun, and S. Lei, Study on the Adhesion and Tribological Behavior of PVD TiAlN Coatings with a Multi-scale Textured Substrate Surface, *Int. J. Refract. Met. Hard.*, 2018, **72**, p 292-305
 27. X. Zhan, P. Yi, Y. Liu, Y. Jiang, Y. Jin, G. Dong, and Y. Zhang, Effects of Texture Spacing and Bulges of Bionic Sinusoidal Texture on the Adhesion Properties and Fracture Mechanism of Plasma-Sprayed Coatings, *Surf. Coat. Technol.*, 2020, **393**, p 125772
 28. S. Costil, H. Liao, A. Gammoudi, and C. Coddet, Influence of Surface Laser Cleaning Combined with Substrate Preheating on the Splat Morphology, *J. Therm. Spray Technol.*, 2005, **14**(1), p 31-38
 29. J. Cedelle, M. Vardelle, and P. Fauchais, Influence of Stainless Steel Substrate Preheating on Surface Topography and on Millimeter- and Micrometer-Sized Splat Formation, *Surf. Coat. Technol.*, 2006, **201**(3), p 1373-1382
 30. L. Zhou, F. Luo, W. Zhou, and D. Zhu, Influence of FeCrAl Content on Microstructure and Bonding Strength of Plasma-Sprayed FeCrAl/Al₂O₃ Coatings, *J. Therm. Spray Technol.*, 2016, **25**(3), p 509-517
 31. W. Xiong and P. Cheng, Numerical Investigation of Air Entrapment in a Molten Droplet Impacting and Solidifying on a Cold Smooth Substrate by 3D Lattice Boltzmann Method, *Int. J. Heat Mass Trans.*, 2018, **124**, p 1262-1274
 32. B. Li, J. Jia, Y. Gao, M. Han, and W. Wang, Microstructural and Tribological Characterization of NiAl Matrix Self-lubricating Composite Coatings by Atmospheric Plasma Spraying, *Tribol. Int.*, 2017, **109**, p 563-570
 33. M.E. Cura, X.W. Liu, U. Kanerva, S. Varjus, A. Kivioja, O. Söderberg, and S. Hannula, Friction Behavior of Alumina/Molybdenum Composites and Formation of MoO₃ - x Phase at 400°C, *Tribol. Int.*, 2015, **87**, p 23-31
 34. N. Tan, Z. Xing, X. Wang, H. Wang, G. Jin, and B. Xu, Investigation of Sprayed Particle Filling Qualities within the Texture on the Bonding Behavior of Ni-Based Coating, *Surf. Coat. Technol.*, 2017, **330**, p 131-139
 35. J. Cai, Q. Guan, P. Lv, X. Hou, Z. Wang, and Z. Han, Adhesion Strength of Thermal Barrier Coatings with Thermal-Sprayed Bondcoat Treated by Compound Method of High-Current Pulsed Electron Beam and Grit Blasting, *J. Therm. Spray Technol.*, 2015, **24**(5), p 798-806
- Publisher's Note** Springer Nature remains neutral with regard to jurisdictional claims in published maps and institutional affiliations.